Detailed Transfer Matrix Method-Based Dynamic Model for Multisection Widely Tunable GCSR Lasers

Olga A. Lavrova, *Student Member, IEEE,* and Daniel J. Blumenthal, *Senior Member, IEEE*

***Abstract*—A theoretical model suitable for both static and dynamic analysis of widely tunable multisection Grating assisted codirectional Coupler with rear Sampled grating Reflector (GCSR) lasers is described in this paper. For the first time wide static tunability as well as transient behavior of such lasers are simulated. The theoretical model is based on the Transfer Matrix Method (TMM) in combination with multimode rate equation analysis and takes into account a number of physical processes in the laser cavity such as longitudinal mode spatial hole burning, nonlinear gain compression, and refractive index changes with carrier injection. Static and dynamic characteristics simulated using the proposed approach agree with the experimental results presented in the paper.**

***Index Terms*—Computer-aided design (CAD) methods and numerical techniques, dynamic wavelength switching, integrated optics and devices, modeling and simulation, tunable semiconductor lasers.**

I. Introduction

WIDELY TUNABLE mutisection lasers are the key components to be employed in future flexible wavelength division multiplexing (WDM) and other network applications (Internet Protocol over WDM (IP-WDM) [1], [2], All-Optical Networking [3], etc.). Grating assisted codirectional coupler with rear sampled grating reflector (GCSR) [4], [5] and sampled-grating DBR (SG-DBR) lasers [6] are the most promising candidates to-date due to their wide tuning range, high side-mode suppression ratio (SMSR), relative simplicity, and potential low cost of fabrication. In order to ensure wavelength agility and failure-free operation, wavelength-tunable devices must not only achieve wide wavelength tuning ranges, but also support stable single-mode operation with high output power and high SMSR for each of these wavelength channels. Furthermore, fast-switching applications like wavelength routing [7] and fast broad-band wavelength conversion [8], [9] will require the shortest possible switching times between different operation channels relatively independent of the start and stop wavelength. To reduce the cost of maintaining these components in the network it is desirable that static and dynamic tuning characteristics of the device stay within the system-driven characteristics throughout the whole operation lifetime. Static, dynamic, and lifetime performance of multisection tunable lasers are sensitive to a considerable number of physical and geometrical parameters so that a powerful theoretical model is desirable for the optimization of complex device structures with respect to ultimate performance and yield.

Several theoretical studies have been performed so far on static and dynamic modeling of multisection DFB and DBR lasers [10]–[12] and some models were presented for widely tunable DBR with periodically sampled and chirped gratings [13]. But no analytical or numerical model has been reported to date for GCSR lasers. In this paper, we present a large-signal dynamic model for GCSR lasers which is based on the Transfer Matrix Method (TMM) in combination with multimode-rate equation analysis and take into account a number of physical processes in the laser cavity such as longitudinal mode spatial hole burning (SHB), nonlinear gain compression, and refractive index changes with carrier injection. This paper studies the wavelength and output power properties of GCSR laser under static and dynamic tuning conditions. The main motivation for this work was to determine the wavelength evolution, amount of crosstalk, and realistic switching times between different wavelength channels at high switching speeds (with $<$ 1-ns risetime) and to compare the obtained results with the experimental ones.

II. Laser Structure

The structure of the multisection GCSR laser is shown in Fig. 1(a). The device consists of four sections: a gain section, followed by a grating-assisted codirectional coupler section, a phase-tuning section, and a reflector section with a sampled DBR (S-DBR). By adjusting the current through the coupler section it is possible to select lasing on one of the reflection peaks of the sampled Bragg grating. The wavelength of the selected Bragg peak and the exact mode position can thereafter be controlled the same as for a conventional DBR laser, i.e., by current injection into the Bragg section and phase section, respectively. Hence, a wide continuous tuning range can be achieved by using all three tuning currents. The laser structure and dimensions are more closely described in [14]. Fig. 1(b) shows superimposed lasing spectra of GCSR operation for a number of ITU grid wavelength channels equally spaced 50 GHz apart. Lasing can be tuned to any wavelength within the tuning range

Manuscript received December 13, 1999; revised June 12, 2000. This work was supported by ONR under Grant N00014-97-1- G024 and under ONR Young Investigator Program Award N00014-97-1- 0987.

The authors are with Optical Communications and Photonic Networks Group, Department of Electrical and Computer Engineering, University of California at Santa Barbara, Santa Barbara, CA 93106 USA (e-mail: olavrova@engineering.ucsb.edu).

Publisher Item Identifier S 0733-8724(00)08071-3.

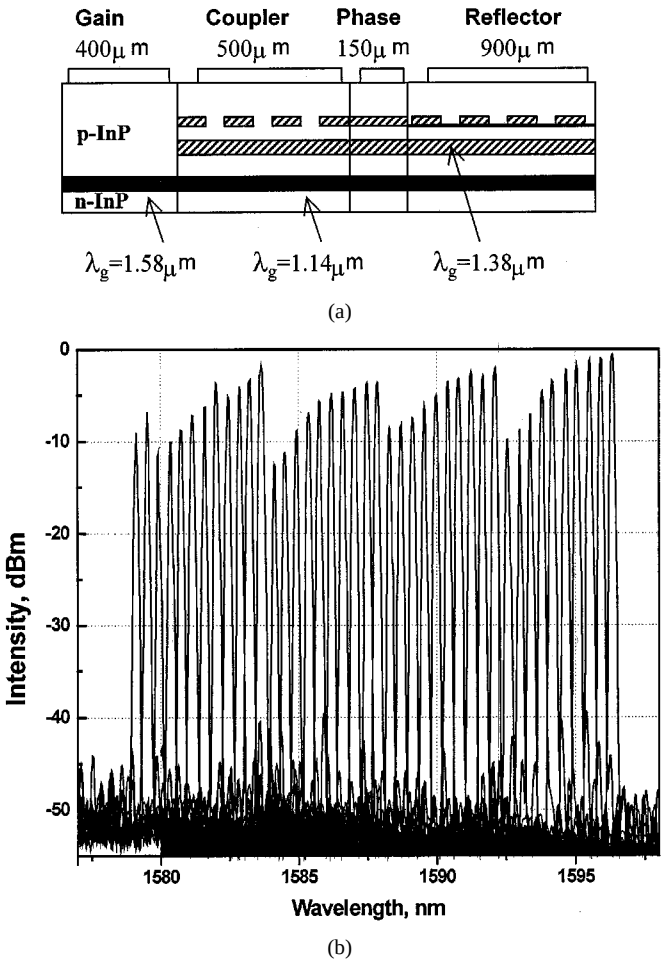

Fig. 1. (a) Schematic structure of the GCSR laser. (b) Experimentally measured superimposed lasing spectra of a large number of 50-GHz-spaced ITU channels.

with $\pm$ 1-GHz accuracy; the widest GCSR tuning range reported so far is 114 nm [14].

III. Model Description and Equations

The model proposed in this paper is based on the TMM [15]. The basis of the TMM is to divide each laser section longitudinally into a number of sections where the structural and material parameters are assumed to be homogeneous throughout each section. However, these parameters may vary between sections, allowing longitudinal inhomogeneities, such as those produced by spatial hole burning, to be incorporated into the model. Each of the sections is characterized by its own 2×2 complex transfer matrix that modifies the forward and backward traveling-wave amplitudes (TWAs) as they propagate through the section. By calculating TWAs of the electric field and solving the multimode photon rate equation, we can solve for transient and steady-state characteristics of the laser. Studies employing the TMM method have to date concentrated mostly on the lasing condition, i.e., values of gain and frequency for which the matrix element $T_{22} = 0$. Our goal is to investigate dynamic as well as static tuning behavior of the GCSR laser, i.e., the values of carrier and photon density together with TWAs at each moment of time in each laser subsection.

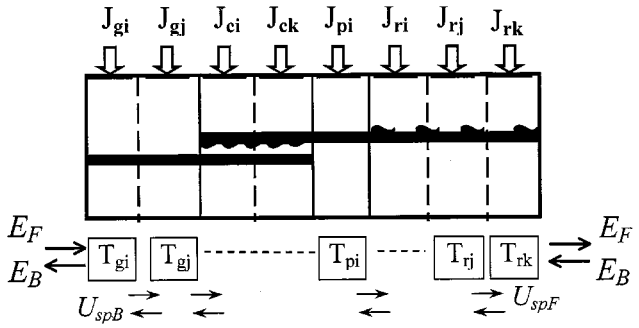

Fig. 2. Schematic illustration of the TMM.

Fig. 2 illustrates the transfer matrix method and shows the forward and backward propagating waves notation. The transfer matrix T for the whole structure is given by a straightforward multiplication of the individual subsection transfer matrices T^{ij}, where the first index stands for the section name (gain, coupler, phase, or reflector), and the second index stands for the number of the subsection within a given section. The forward and backward propagating spontaneous emission is represented by equivalent lumped inputs U_{spF} and U_{spB}, respectively, at the boundaries of each subsection. The steady-state TMM equations for the ij subsection of the laser structure are written as follows:

$$\begin{bmatrix} E_F^{i(j+1)}(\omega) \\ E_B^{i(j+1)}(\omega) \end{bmatrix} = \begin{bmatrix} T_{11}^{ij}(\omega) & T_{12}^{ij}(\omega) \\ T_{21}^{ij}(\omega) & T_{22}^{ij}(\omega) \end{bmatrix} \cdot \begin{bmatrix} E_F^{ij}(\omega) \\ E_B^{ij}(\omega) \end{bmatrix} + \begin{bmatrix} U_{spF}^{i(j+1)}(\omega) \\ U_{spB}^{i(j+1)}(\omega) \end{bmatrix} \quad (1)$$

where E_F^{ij} and E_B^{ij} are the forward and reverse propagating TWAs of the ij subsection. The boundary conditions at the ends of the waveguide ($z = 0$ and $z = L$) are

$$E_F(\omega, 0) = r_f \cdot E_B(\omega, 0) \text{ and } E_B(\omega, L) = r_b \cdot E_F(\omega, L)$$

where r_f and r_b are the amplitude facet reflectivities.

However, the time-independent TMM equations above have to be modified in order to be employed in the time-dependent case. In this particular case, (1) will look as follows (omitting the spontaneous emission terms for simplicity):

$$\begin{bmatrix} E_F^{i(j+1)}(\omega, t+\Delta t) \\ E_B^{i(j+1)}(\omega, t) \end{bmatrix} = \begin{bmatrix} T_{11}^{ij}(\omega, t) & T_{12}^{ij}(\omega, t) \\ T_{21}^{ij}(\omega, t) & T_{22}^{ij}(\omega, t) \end{bmatrix} \cdot \begin{bmatrix} E_F^{ij}(\omega, t) \\ E_B^{ij}(\omega, t+\Delta t) \end{bmatrix}. \quad (2)$$

Rearranging these equations produces expressions for the updated amplitudes in terms of the old wave amplitudes and the transfer matrix elements

$$E_B^{ij}(\omega, t+\Delta t) = \frac{1}{T_{22}^{ij}(t)} \left(E_B^{i(j+1)}(\omega, t) - T_{21}^{ij}(t) \cdot E_F^{ij}(\omega, t) \right) \quad (3a)$$

$$E_F^{i(j+1)}(\omega, t+\Delta t) = \left(T_{11}^{ij}(t) \cdot E_F^{ij}(\omega, t) + T_{12}^{ij}(t) \cdot E_B^{ij}(\omega, t+\Delta t) \right). \quad (3b)$$

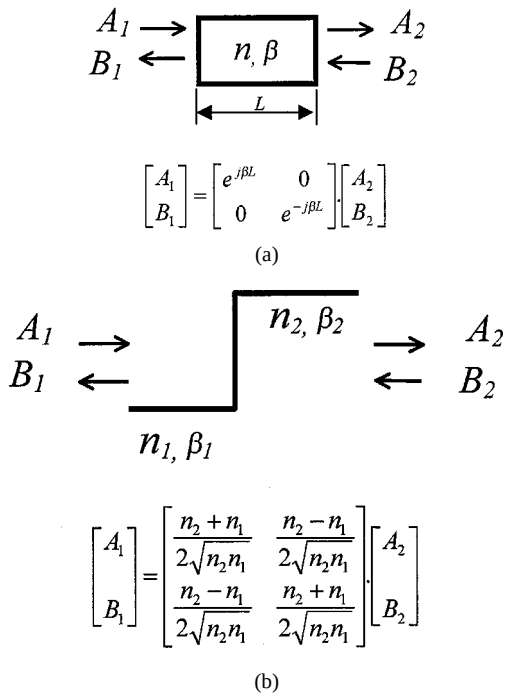

Fig. 3. Basic transmission matrices for (a) homogeneous waveguide and (b) refractive index step.

Here we should note that all of the subsections must have the same length equal to $\Delta z = v_g \Delta t$ where v_g is the group velocity. In addition to ensuring that SHB effects are included, subdividing each section into further subsections ensures that the basic assumption of the time-dependent TMM is satisfied, i.e., transfer matrices of each subsection $[T_k(t)]$ remain unchanged over the interval t to $t + \Delta t$.

The transfer matrices associated with the elementary subsections can normally be found in a straightforward manner. Fig. 3(a) and (b) show the most basic transmission matrices associated with a homogeneous waveguide of length L with a complex propagation constant β [Fig. 3(a)] and a refractive index step from n_1 to n_2 [Fig. 3(b)]. From just these two structures it is possible to build a wide range of laser structures. The transfer matrix for the gain section is given simply by the product of transfer matrices for homogeneous waveguides

$$[T_{gain}] = [T_{g,i}] \cdot [T_{g,j}] \cdot \cdots \cdot [T_{g,m}] = \prod_{i=1}^{m} [T_{g,i}] \quad (4)$$

where m is the number of subsections in the gain section. A similar formula can be written for the phase section.

In order to derive the transfer matrix for the sampled reflector we need to consequently multiply the transfer matrices corresponding to the corrugation periods with the matrices corresponding to the propagation in the homogeneous waveguide regions [see Fig. 4(a)]. The difficulty of the chirped sampled reflector case from the point of view of numerical calculations is that the refractive index profile is different within different subsections. That means that a sophisticated meshing subroutine has to be designed for this section. Derivation of the transmission matrix for the sampled reflector is demonstrated in the Appendix. Here, for the sake of simplicity, we show the general form of the sampled reflector transfer matrix for the static case;

$$\begin{bmatrix} E_F^{r,M}(\omega) \\ E_B^{r,M}(\omega) \end{bmatrix} = \prod_{j=1}^{M} \left(\left[T_{\text{grating}}^{r,j}(\omega) \right] \cdot \left[T_{\text{space}}^{r,j}(\omega) \right] \right) \cdot \begin{bmatrix} E_F^{r,0}(\omega) \\ E_B^{r,0}(\omega) \end{bmatrix} \quad (5)$$

where $T_{\text{grating}}^{r,j}$ and $T_{\text{space}}^{r,j}$ are the 2×2 transfer matrices of the grating burst and uncorrugated space for the jth subsection of the reflector section, M is the total number of sampled periods.

Until now we were dealing with the sections that had only one waveguide, i.e., they were considered as a two-port problem with 2×2 characteristic transfer matrices. This is not the case with the coupler section, which has to be treated as a four-port with a corresponding 4×4 transfer matrix. The transfer matrix for a single corrugation period in static case [see Fig. 4(b)] will look as follows:

$$\begin{bmatrix} E_{F_1}^{c,N}(\omega) \\ E_{B_1}^{c,N}(\omega) \\ E_{F_2}^{c,N}(\omega) \\ E_{B_2}^{c,N}(\omega) \end{bmatrix} = \prod_{j=1}^{N} \left(\left[O_{12}^{c,j}(\omega) \right] \cdot \left[T_{(\omega)}^{c,j} \right] \cdot \left[O_{21}^{c,j}(\omega) \right] \cdot \left[T_1^{c,j}(\omega) \right] \right) \cdot \begin{bmatrix} E_{F_1}^{c,0}(\omega) \\ E \\ E_{F_2}^{c,0}(\omega) \\ E_{B_2}^{c,0}(\omega) \end{bmatrix} \quad (6)$$

where $T_1^{c,j}$, $T_2^{c,j}$ are the 4×4 propagation matrices for high or low reflection index region of the corrugation in the jth subsection of the reflector, $O_{12}^{c,j}$, $O_{21}^{c,j}$ are the 4×4 overlap matrix for the interface between high or low reflection index waveguides, and N is the number of corrugation periods in the coupler section. Derivation and details of these matrices are given in the Appendix.

Finally, (4)–(6) are used to find the overall transfer matrix of the whole GCSR laser structure. In the static case, transmission of the lasing mode tends to infinity if the net gain equals the threshold gain g_{th} and the wavelength corresponds to a lasing wavelength of the cavity. For the dynamic case, following the algorithm described by (3), we can find the TWAs of the forward and reverse propagating electric field at each moment of time, and derive carrier and photon distributions together with output power and lasing wavelength at each moment of time. No assumptions were used in any of the above equations, so they may successively be employed for both large- and small-signal analysis.

As has been mentioned before, each of the subsections is characterized by a constant carrier density, photon density, effective refractive index, phase shift, and coupling coefficient for the coupler and reflector sections. Within a section i the local interaction between the carrier density N^{ij} and the photon densities S_p^{ij} of the longitudinal mode p is described by the multimode photon rate equation

$$\frac{dN^{ij}}{dt} = \eta \frac{I^{ij}}{eV_i} - AN^{ij} - B(N^{ij})^2 - C(N^{ij})^3 - \sum_{p=1}^{P} v_g g^{ij} S_p^{ij}. \quad (7)$$

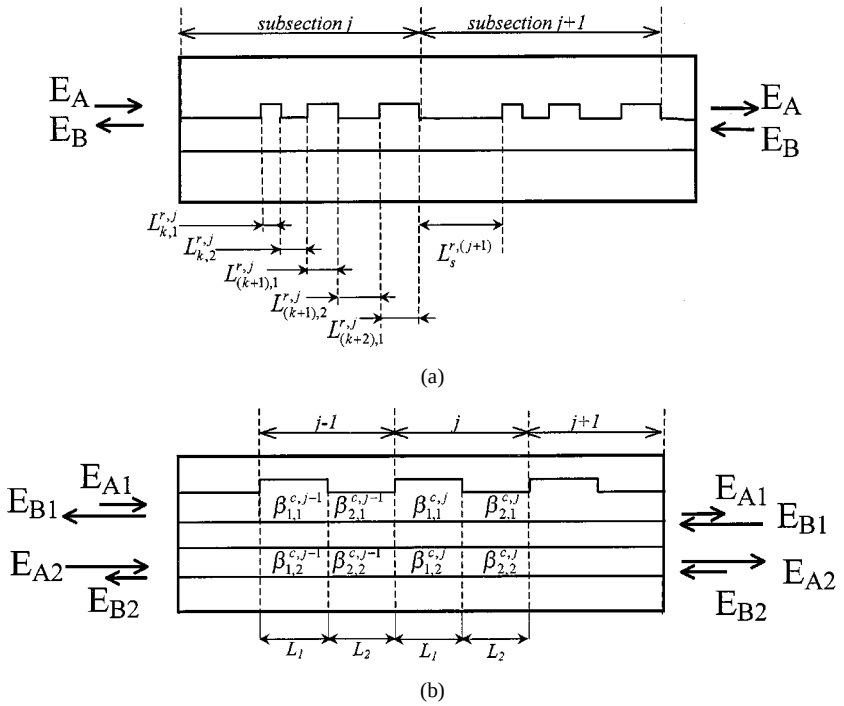

Fig. 4. Illustration to obtaining the transfer matrices for (a) sampled reflector and (b) grating-assisted coupler.

Here I^{ij} denotes the current injected in each subsection, η is the injection efficiency of current into the active volume V^{ij}, e is the electron charge, g^{ij} is the power material gain, P is the number of axial modes in the multimode case, and A, B, C are parameters describing nonradiative, bimolecular, and Auger recombination, respectively. The photon density for each mode p in each subsection is given by

$$S_p^{ij} = \left(\left| E_{F,p}^{ij} \right|^2 + \left| E_{B,p}^{ij} \right|^2 \right) \frac{1}{2v_g}. \tag{8}$$

The power material gain is approximated by the standard linear function of the carrier density with a slope given by the differential gain dg/dN and an offset defined by the transparency carrier density N_{tr}

$$g_p^{ij}(N^{ij}, S_p^{ij}) = \frac{\dfrac{dg}{dN}(N^{ij} - N_{tr})}{1 + \varepsilon S_p^{ij}} \tag{9}$$

where ε is the gain compression factor. The refractive index of the waveguide $n_{act,i}$ in section i as a first approximation linearized around the transparency carrier density using the linewidth enhancement factor α

$$n_{\text{act}}^{ij}(N^{ij}) = n_{\text{act}}^{ij} - \frac{1}{4\pi}\frac{dg}{dN}\alpha\lambda(N^{ij} - N_t). \tag{10}$$

The variation of the effective refractive index Δn_{eff} is obtained from the refractive index change Δn_{act} in the active layer using the approximation, which can be obtained by first-order perturbation theory

$$\Delta n_{\text{eff}} \cong \Gamma_p \Delta n_{\text{act}} \tag{11}$$

where γ_p is the optical confinement factor of the active layer for the pth mode.

In the steady-state case, the TMM algorithm computes the self-consistent solution for the longitudinal distributions of the carrier density, photon density, and the carrier-induced refractive index change at a particular bias level. Laser tuning curves are calculated as the peak lasing wavelengths assuming the steady-state carrier, photon and refractive index distributions. The time-averaged output spectrum of the laser is calculated as the power out of the front facet

$$P(\omega, t) = (1 - R_f)hv \cdot wd\left|E_{B1}(\omega, t)\right|^2 \tag{12}$$

where R_f is the reflection coefficient of the front facet, hv is the photon energy, and w and d are active region width and thickness, respectively.

The block diagram of the transient calculation is shown in Fig. 5. First, the structure is initialized with either zero-current state or any other state that could be saved from previous calculations, and the uniform or nonuniform mesh is set up over all the sections of the laser. Then for each section, given the new value of currents, the subsection carrier densities N^{ij} are calculated according to the carrier-density rate equation (7), this in its turn updates the values of refractive index and gain for each subsection according to (9) and (10). On the next step, new values for the transfer matrices for each subsection are calculated and the values of the forward- and reverse-propagating traveling waves are updated. The photon density for each subsection is calculated and the output power from the front facet is found. The procedure is carried out for the desired number of wavelength points, after which the whole procedure starts all over again with new values of time and current.

In our transient process studies we were primarily concerned with switching between different lasing modes, which involves changing only the values of the coupler, reflector, and phase sections keeping the gain current constant. Our primary goal was

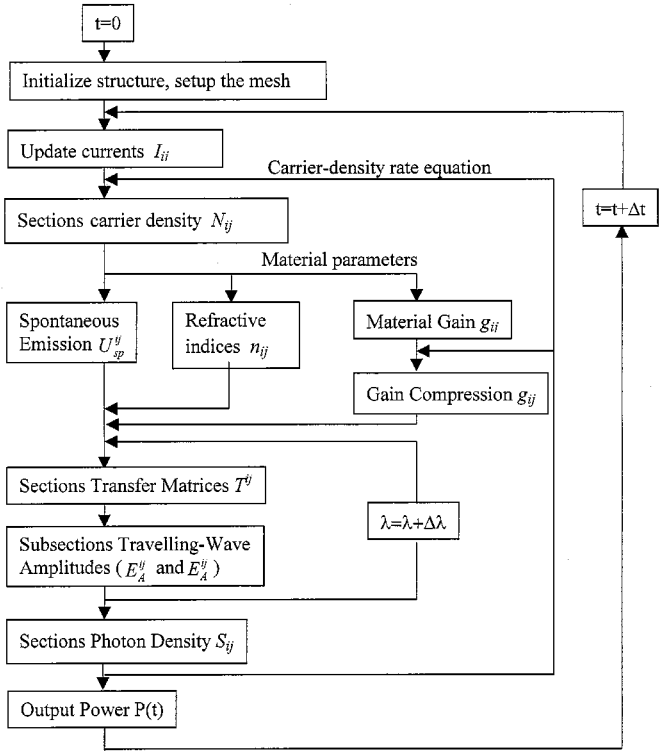

Fig. 5. Block diagram of the transient calculation procedure.

to study the evolution of the wavelength and the switching time as a function of switching modes and to identify the factors that could help improve dynamic tuning performance. The results are described in the following sections.

IV. Static Results

To demonstrate and verify the model, we have performed static analysis of the optical spectra, lasing wavelength, and tuning curves of a typical four-section GCSR laser. The material and geometrical parameters of the simulated device are given in Table I. All calculations are performed on the Pentium III personal computer. Typical computing times were on the order of 10 h (depending on the problem conditions).

The tuning curves of a GCSR laser are an essential point for the comparison between theory and experiment, since the position and relative amplitudes of various modes are sensitively influenced by the structure and waveguide parameters, the coupling factor, the phase shifts, and the unknown end facet phases of the grating. Static tuning curves for the simulated device are shown in Fig. 6(a) and (b). Coarse tuning of the lasing wavelength is realized by changing only coupler current—peak wavelength is tuned in steps corresponding to sampled reflector comb spacing (4–6 nm). Medium tuning is realized by changing reflector current—peak wavelength is changed in jumps corresponding to longitudinal mode spacing of the GCSR laser cavity (0.2–0.4 nm). Truly continuous tuning of the lasing wavelength is realized by simultaneous changes of all three (coupler, reflector, and phase) currents (not shown in the figure for clarity). Fig. 6(a) shows the wavelength surface that can be obtained by tuning of the device with both coupler and reflector currents. Fig. 6(b) is a two-dimensional (2-D) cross section of the plot

TABLE I
Parameters Used in Simulation

Parameter	Unit	Value
Gain section length, L_g	μm	500
Waveguide thickness, d	μm	0.2
Waveguide width, w	μm	1.5
Active section waveguide loss, α	cm^{-1}	40
Active section group index, n_g	-	4
Gain compression parameter, ε	cm^{-3}	$1.5x10^{-17}$
Transparency carrier density, N_{tr}	cm^{-3}	$1.15x10^{18}$
Differential gain, dg/dN	cm^2	$2x10^{-16}$
Coupler section length, L_c	μm	500
Coupler center wavelength at zero bias, λ_c	μm	1.605
Tuning efficiency, dn/dN	cm^{-3}	$-17x10^{-21}$
Reflector section length, L_r	μm	900
Reflector center wavelength at zero bias, λ_r	μm	1.605
Phase section length, L_p	μm	150
Non-radiative recombination coeff., A	s^{-1}	$0.5x10^8$
Radiative recombination coeff., B	cm^3s^{-1}	$1x10^{-10}$
Auger recombination coeff., C	cm^6s^{-1}	$2.5x10^{-29}$

in Fig. 6(a) and shows tuning curves as a function of only reflector current with coupler current fixed at different values. The peak lasing wavelength is plotted for each pair of coupler and reflector currents with the SMSR $\geq$ 30-dB criteria, so that no point is plotted in case of multimode operation or if the SMSR is less then 30 dB. From the plot we can see that some wavelengths are impossible to obtain or can only be obtained with a poor SMSR—as can be anticipated, this happens when the sampled reflector and grated coupler transmission spectras have poor or no overlap. Most of these wavelengths can still be reached when tuning with phase current is also used. A separate plot would be needed to illustrate this since the phase current would correspond to another dimension.

Fig. 7(a) and (b) shows experimentally measured tuning curves, similar to the simulated ones in Fig. 6. Wavelength positions of the plateaus are in good agreement with the simulated ones. A larger number of wavelengths is missing on the measured tuning curve then it was predicted in the simulation. This may be due to any imperfections of the GCSR fabrication that are difficult to account for in the simulation (such as waveguide thickness deviations, overgrowth imperfections, etc).

V. Dynamic Results

A. Transient Process

Fig. 8 shows the calculated transient turn-on process from $I = 0$ mA to $I = 3I_{th}$ for the two characteristic cases. In Fig. 8(a), the final state corresponds to a stable single-mode operation, and in Fig. 8(b), the final state corresponds to multimode

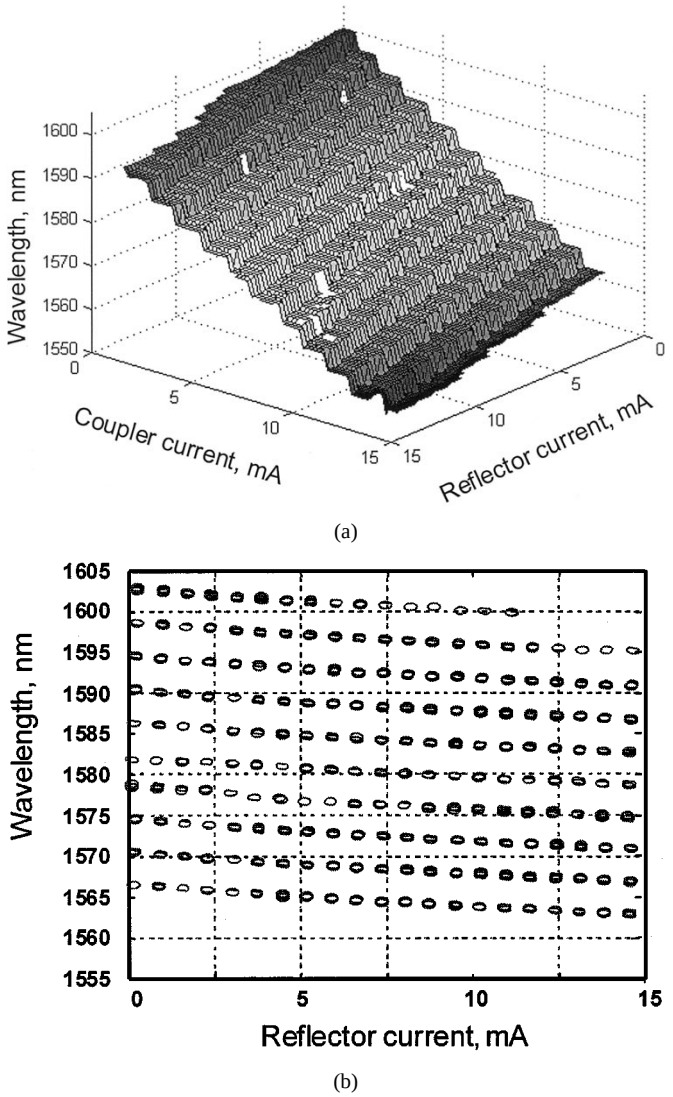

Fig. 6. Static tuning curves of the GCSR laser, showing all possible lasing wavelengths. (a) Three–dimensional (3-D) surface obtained by variation of both coupler and reflector currents. (b) Cross section of (a) obtained by variation of the reflector current at fixed values of the coupler current.

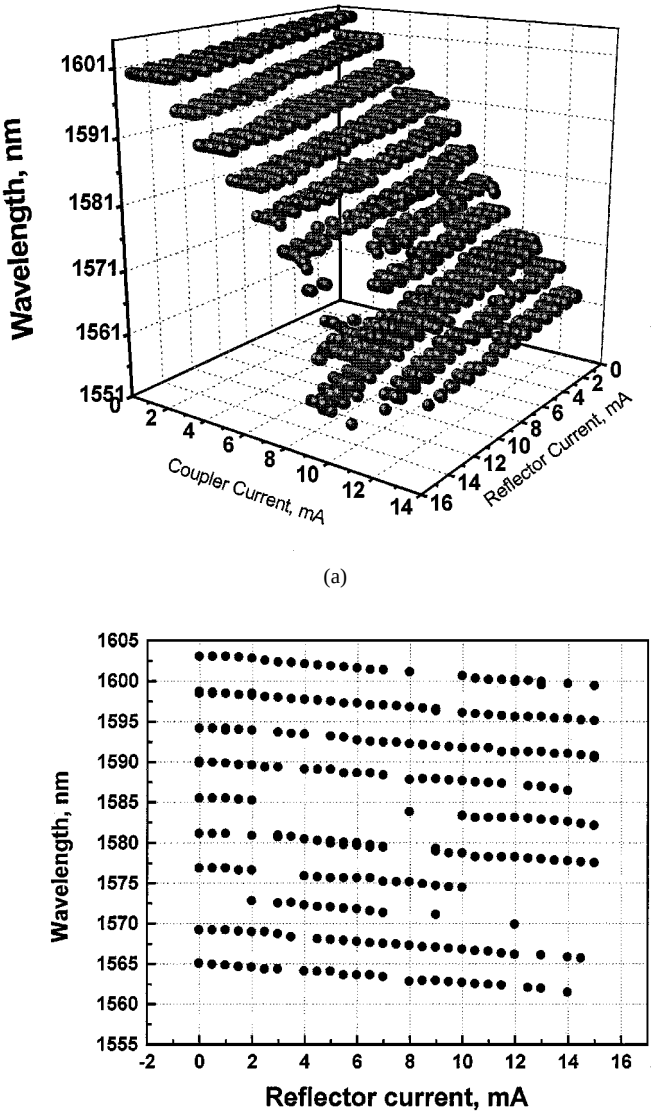

Fig. 7. Experimentally measured static tuning curves of the GCSR laser.

operation. In case of Fig. 8(a), the peak lasing mode is selected and all other modes are suppressed from the very beginning. The case of Fig. 8(b) shows the worst case of the mode competition when both modes come up initially, but the shorter wavelength mode is then slowly suppressed. The side-mode suppression time depends on the initial (zero coupler and zero reflector currents) alignment of the coupler and reflector peaks, which in many cases is determined by the unknowns of the technological process (relative phase of the rear facet reflection, phase shift and amplitude of the internal reflections, etc).

B. Dynamic Wavelength Switching

Optical network applications require access to a large number of channels and the latency of such networks is determined by the switching time between different channels. Thus it is important to study and optimize the wavelength-switching behavior before the laser is employed in a fast optical network.

As was mentioned before, tuning is obtained by changing either coupler, reflector, or phase current, or all of them together while keeping gain current constant (such that coupler, reflector, and/or phase sections carrier densities are changed directly, while the carrier density in the gain section is allowed to vary as a result of these changes). In the case of carrier-induced index change, the carrier-density response to a current step can be approximated by the exponential function [16]

$$N(t) = N_{\text{start}} + (N_{\text{stop}} - N_{\text{start}}) \left(1 - \exp\left(-\frac{t}{\tau_s}\right)\right) \quad (13)$$

where N_{start} and N_{stop} are initial and final carrier concentrations, τ_s—spontaneous recombination time. It can be clearly seen that the switching time will depend on N_{start} and N_{stop}. Also, depending on the initial and final wavelengths, lasing on this wavelength is characterized by a certain carrier density interval

$$N(\lambda_i) = N_i \pm \Delta N_i. \quad (14)$$

The switching time will vary considerably between switching of the $\lambda_0 \leftrightarrow \lambda_1$ wavelength channels and $\lambda_0 \leftrightarrow \lambda_{10}$ (where

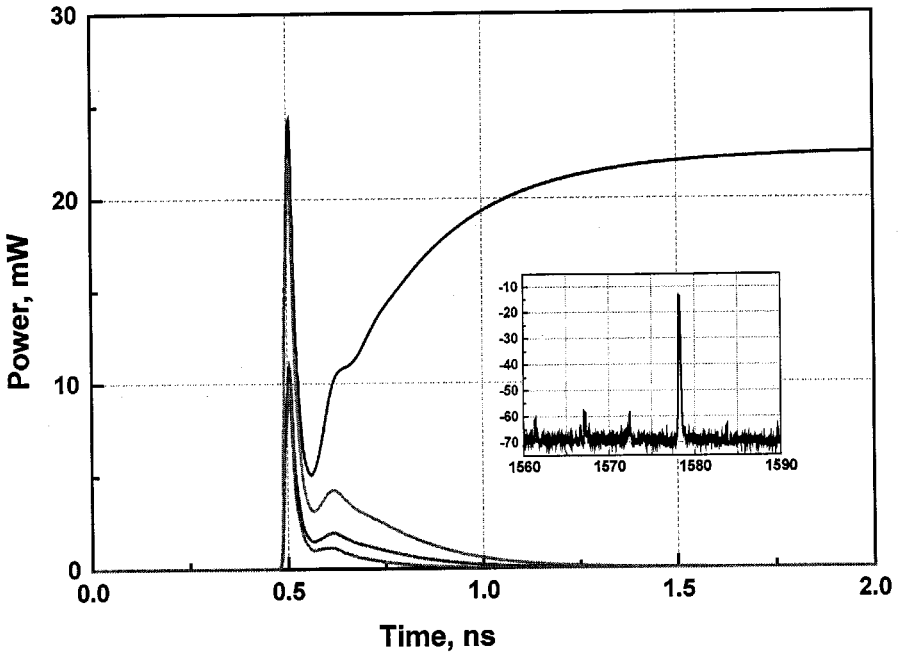

(a)

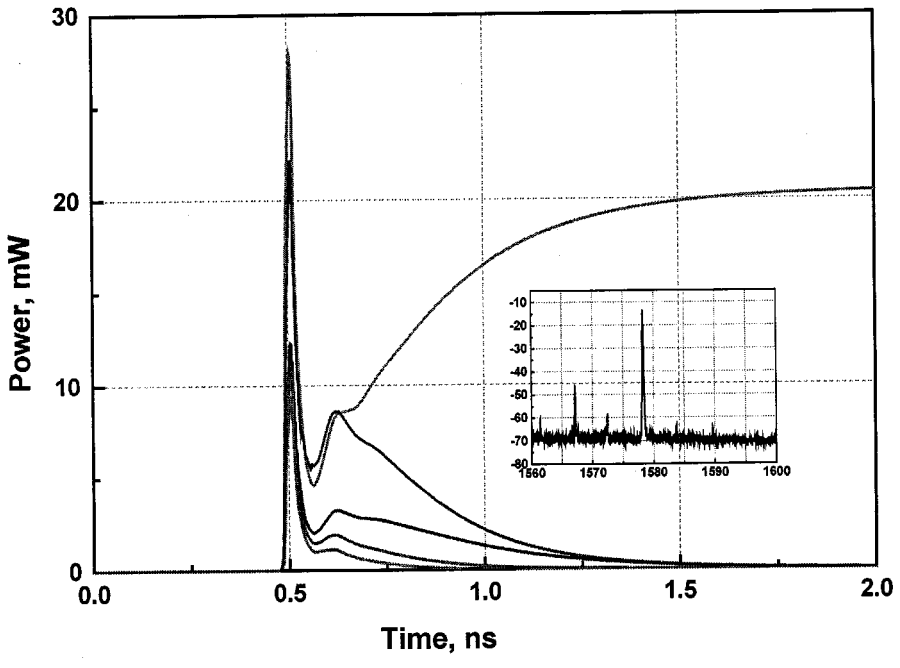

(b)

Fig. 8. Transient turn-on process for (a) stable single-mode operation and (b) multimode operation regimes.

wavelength 0 through 10 are numbered sequentially. This is illustrated in Fig. 9.

We performed simulations of the wavelength switching between a large number of wavelength channels. The upper curve in Fig. 10 shows the simulated waveforms for the case of switching between two different wavelength channels λ_4 and λ_8 which are 20 nm (or three wavelength channels) apart. The switching time is 6.5 ns for the $\lambda_4 \rightarrow \lambda_8$ transition and 5.5 ns for the $\lambda_8 \rightarrow \lambda_4$ transition. A significant amount of interchannel crosstalk noise (momentary spikes of signal at intermediate wavelengths λ_5, λ_6, and λ_7) is observed during the transient time. Lasing at these intermediate wavelengths is due to the fact that the carrier density is swept through the whole range of values corresponding to each of these channels. The switching time may be reduced if the shape of the driving current pulse is modified from square to a differentiated rise and fall fronts [17]. Simulated waveforms for the same $\lambda_4 \leftrightarrow \lambda_8$ switching but with modified current pulses are shown in the lower waveform in Fig. 10. The switching times have now decreased to 4.9 and 4 ns for the $\lambda_4 \rightarrow \lambda_8$ and $\lambda_8 \rightarrow \lambda_4$ transitions, respectively. It can be clearly seen that the amount of transient interchannel crosstalk is much smaller and the switching time

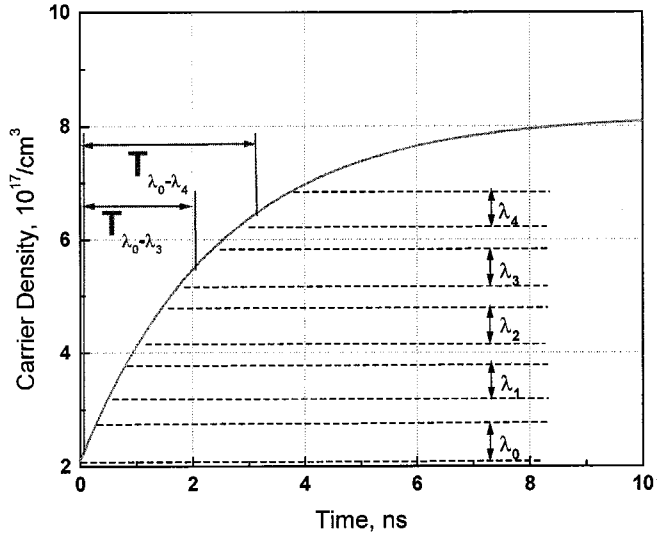

Fig. 9. Carrier density response to a current step and carrier density ranges, corresponding to different lasing wavelengths λ_i.

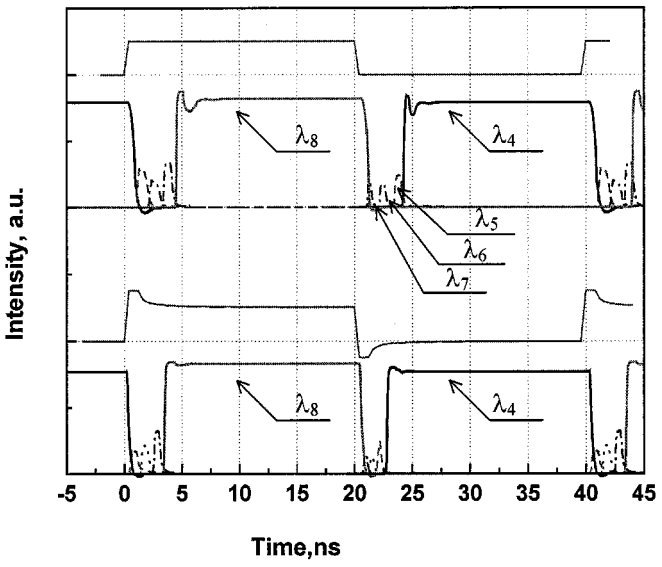

Fig. 10. Simulated switching waveforms for switching between λ_4 and λ_8.

is much shorter in this case. Simulated switching time as a function of a wavelength number for the case of square driving pulses and differentiated pulses is shown in Fig. 11. The logarithmic increase of the switching time is observed in both cases as the wavelength step increases. However, using the predistortion differentiated pulses, we could measure a significant reduction of the switching time.

Fig. 12(a) shows measured switching waveforms for switching between two lasing modes 20 nm apart (similar to the one shown in Fig. 10) using the predistortion technique. The switching times were found to be 7.6 and 6.2 ns (compare to 4.9 and 4 ns as simulated). The amount of the interchannel crosstalk measured in the experiment is larger than predicted in the simulation, and is due to the parasitics in the experimental circuitry. Fig. 12(b) shows measured switching time as a function of a wavelength number, similar to the one in the Fig. 11. Details of this switching experiment are described

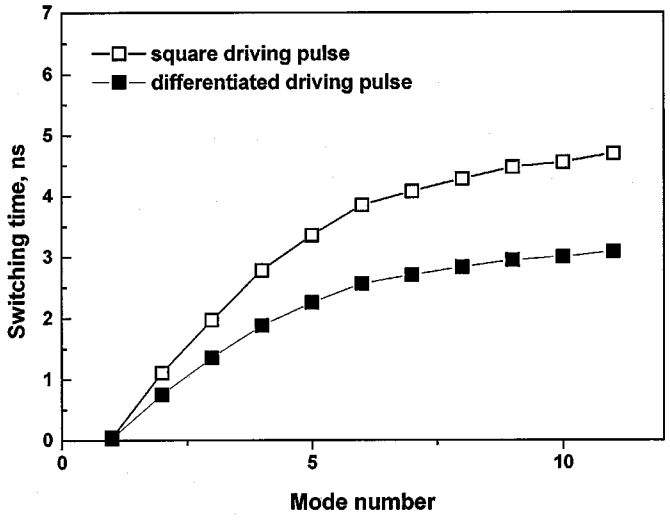

Fig. 11. Calculated switching times for switching between different wavelengths $\lambda_N \rightarrow \lambda_0$.

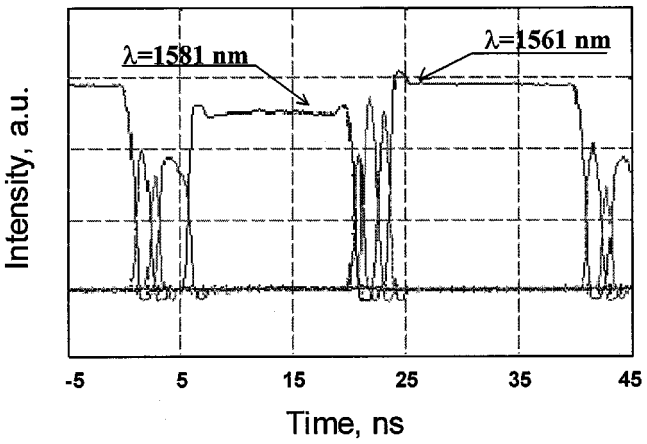

(a)

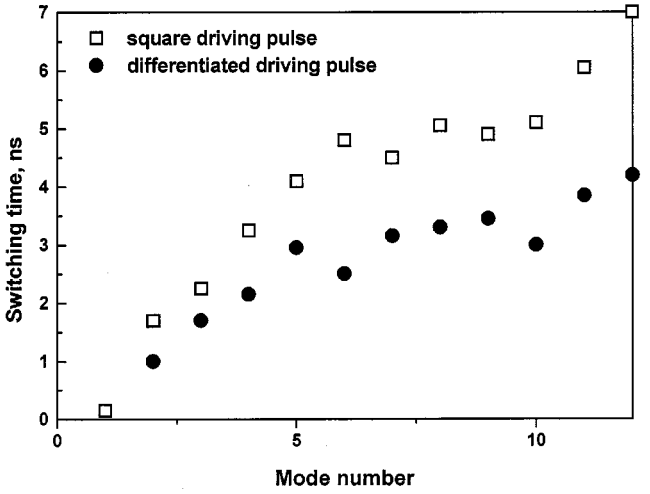

(b)

Fig. 12. Measured (a) switching waveforms and (b) switching times for the $\lambda_N \rightarrow \lambda_0$ transition.

in [17], where switching time reduction up to 50%, using the predistorted pulses, was reported. The measured and calculated

switching times show a good agreement demonstrating the validity of the proposed dynamic model.

VI. Conclusion

A new dynamic transfer-matrix-based model in application for widely tunable GCSR lasers is developed and described in this paper. Static and dynamic tuning, transient process dynamics, and switching time were simulated and compared with the experiment. This model gives accurate self-consistent results that agree well with the measured ones.

The proposed model may find several applications such as design of the GCSR laser structures aimed to optimize device ultimate performance or analysis of similar types of lasers (like sampled-grating DBRs). The efficiency of the numerical simulation (which runs easily on a personal computer) suggests that the proposed model can be used as a building block in CAD programs analyzing reconfigurable multiwavelength optical network systems.

Appendix

This Appendix presents the description and derivation of the transfer matrices for a grating-assisted coupler and chirped sampled reflector. For the sake of simplicity we will consider the generic case when the length of the subsection Δz equals exactly one period of either coupler or reflector section. This is not always true since Δz is determined by the time step of the analysis Δt, but generalization of the obtained equations to a case when Δz contains more then one or less then one period can be done in a fairly straightforward manner.

A. Transmission Matrix for the Chirped Sampled Reflector

The schematic view of one period of the sampled reflector is shown in Fig. 4(a). As was stated in (5), the total transmission matrix of the sampled reflector is

$$\begin{bmatrix} E_F^{r,M}(\omega) \\ E_B^{r,M}(\omega) \end{bmatrix} = \prod_{j=1}^{M} \left(\left[T_{\text{grating}}^{r,j}(\omega) \right] \cdot \left[T_{\text{space}}^{r,j}(\omega) \right] \right) \cdot \begin{bmatrix} E_F^{r,0}(\omega) \\ E_B^{r,0}(\omega) \end{bmatrix} \tag{5}$$

where M is the total number of sampled periods and T_g is the transmission matrix of the grating burst

$$T_{grating}^{r,j}(\omega) = \prod_{k=1}^{K} T_k^{r,j}(\omega) \tag{5a}$$

where $T_k^{r,j}(\omega)$ is the transmission matrix of each of the kth corrugation period in the ith subsection which can be written as follows (omitting r and j indexes for simplicity):

$$T_k(\omega) = \begin{bmatrix} \frac{n_2+n_1}{2\sqrt{n_2 n_1}} & \frac{n_2-n_1}{2\sqrt{n_2 n_1}} \\ \frac{n_2-n_1}{2\sqrt{n_2 n_1}} & \frac{n_2+n_1}{2\sqrt{n_2 n_1}} \end{bmatrix} \cdot \begin{bmatrix} e^{j\beta_{k1}L_{k1}} & 0 \\ 0 & e^{-j\beta_{k1}L_{k1}} \end{bmatrix} \cdot \begin{bmatrix} \frac{n_2+n_1}{2\sqrt{n_2 n_1}} & \frac{n_1-n_2}{2\sqrt{n_2 n_1}} \\ \frac{n_1-n_2}{2\sqrt{n_2 n_1}} & \frac{n_2+n_1}{2\sqrt{n_2 n_1}} \end{bmatrix} \cdot \begin{bmatrix} e^{j\beta_{k2}L_{k2}} & 0 \\ 0 & e^{-j\beta_2 L_{k2}} \end{bmatrix} \tag{5b}$$

and $T_{\text{space}}^{r,j}(\omega)$ is the transmission matrix of the uncorrugated space in the ith subsection

$$T_{\text{space}}^{r,j}(\omega) = \begin{bmatrix} e^{j\beta_1^{r,j}L_s^{r,j}} & 0 \\ 0 & e^{-j\beta_1^{r,j}L_s^{r,j}} \end{bmatrix} \tag{5c}$$

where n_1, n_2, L_{k1}, L_{k2}, β_{k1}, and β_{k2} are refractive indexes, length, and propagation constants for the high and low refractive index corrugation regions ($k = 1, 2$); correspondingly, L_s is the length of the unsampled region.

B. Transmission Matrix for the Grating-Assisted Coupler

A schematic view of the grating-assisted coupler is shown in Fig. 4(b). As was stated in (6), the total transmission matrix of the grating-assisted coupler is

$$\begin{bmatrix} E_{F_1}^{c,N}(\omega) \\ E_{B_1}^{c,N}(\omega) \\ E_{F_2}^{c,N}(\omega) \\ E_{B_2}^{c,N}(\omega) \end{bmatrix} = \prod_{j=1}^{N} \left(\left[O_{12}^{c,j}(\omega) \right] \cdot \left[T_2^{c,j}(\omega) \right] \cdot \left[O_{21}^{c,j}(\omega) \right] \cdot \left[T_1^{c,j}(\omega) \right] \right) \cdot \begin{bmatrix} E_{F_1}^{c,0}(\omega) \\ E \\ E_{F_2}^{c,0}(\omega) \\ E_{B_2}^{c,0}(\omega) \end{bmatrix} \tag{6}$$

where N is the number of corrugation periods in the coupler section, $T_1^{c,j}$ and $T_2^{c,j}$ are 4×4 propagation matrices for high- or low- reflection index region of the corrugation in the jth subsection of the reflector which can be written as in (6a) at the bottom of this page (omitting c and j indexes for simplicity) where $\beta_{k,p}$ is the propagation constant for the high- and low-refractive index corrugation regions ($k = 1, 2$) in the upper or lower waveguide ($p = 1, 2$) respectively. $O_{12}^{c,j}$ and $O_{21}^{c,j}$ are the 4×4 overlap matrices for the mode matching at the interface between

$$T_1 = \begin{bmatrix} \exp(j\beta_{1,1}L_1) & 0 & 0 & 0 \\ 0 & \exp(-j\beta_{1,1}L_1) & 0 & 0 \\ 0 & 0 & \exp(j\beta_{1,2}L_1) & 0 \\ 0 & 0 & 0 & \exp(-j\beta_{1,2}L_1) \end{bmatrix} \tag{6a}$$

high- or low-reflection index waveguides, such that (omitting c and j indexes for simplicity again)

$$O_{12} = \begin{bmatrix} \langle 1|1\rangle & 0 & \langle 1|2\rangle & 0 \\ 0 & \langle 1|1\rangle & 0 & \langle 1|2\rangle \\ \langle 1|2\rangle & 0 & \langle 1|1\rangle & 0 \\ 0 & \langle 1|2\rangle & 0 & \langle 1|1\rangle \end{bmatrix} \tag{6b}$$

where $1, 2$ stand for upper and lower waveguide, and $\langle 1|1\rangle$ and $\langle 1|2\rangle$ are overlap integrals at the interface between high- and low-refractive index regions. Calculation of these integrals is described elsewhere [18] and is beyond the scope of this paper.

ACKNOWLEDGMENT

Authors wish to thank Dr. G. Rossi for fruitful discussions and Dr. J. Piprek for valuable comments.

REFERENCES

[1] D. Chiaroni, B. Lavigne, A. Jourdan, M. Sotom, L. Hamon, C. Chauzat, J.-C. Jacquinot, A. Barroso, T. Zami, F. Dorgeuille, C. Janz, J.-Y. Emery, E. Grard, and M. Renaud, "Physical and logical validation of a network based on all-optical packet switching systems," *J. Lightwave Technol.*, vol. 16, no. 12, pp. 2255–2264, Dec. 1998.

[2] P. Gambini, M. Renaud, C. Guillemot, F. Callegati, I. Andonovic, B. Bostica, D. Chiaroni, G. Corazza, S. L. Danielsen, P. Gravey, P. B. Hansen, M. Henry, C. Janz, A. Kloch, R. Krahenbuhl, C. Raffaelli, M. Schilling, A. Talneau, and L. Zucchelli, "Transparent optical packet switching: network architecture and demonstrations on the KEOPS project," *IEEE J. Select. Areas Commun.*, vol. 16, pp. 1245–1259, Sept. 1998.

[3] M. Shell, M. D. Vaughn, L. Dubertrand, D. J. Blumenthal, P. J. Rigole, and S. Nilsson, "Multi-node demonstration of a multihop wavelength-routed all-optical packet switched network (MMPONet)," in *Optical Fiber Communications Conf. (OFC '97)*, vol. 6, Dallas, TX, Feb. 16–21, 1997, paper TuR2.

[4] P. J. Rigole, S. Nilsson, E. Berglind, D. J. Blumenthal, and M. Shell, "State of the art; Widely tunable lasers," in *SPIE-Int. Soc. Opt. Eng.*, vol. 3001, San Jose, CA, Feb. 10–13, 1997, pp. 382–393.

[5] P.-J. Rigole, S. Nilsson, T. Klinga, L. Bäckbom, B. Stalnacke, E. Berglind, B. Stoltz, D. J. Blumenthal, and M. Shell, "Wavelength coverage over 67 nm with a GCSR laser tuning characteristics and switching speed," presented at the Optical Fiber Communication Conf. (OFC '97), Dallas, TX, Feb. 1997, Paper WL63.

[6] B. Mason, S. P. DenBaars, and L. A. Coldren, "Tunable sampled-grating DBR lasers with integrated wavelength monitors," *IEEE Photon. Technol. Lett.*, vol. 10, pp. 1085–1087, Aug. 1998.

[7] R. Gaudino, M. Len, G. Desa, M. Shell, and D. J. Blumenthal, "MOSAIC: A multiwavelength optical subcarrier multiplexed controlled network," *IEEE J. Select. Areas Commun.*, vol. 16, pp. 1270–1285, Sept. 1998.

[8] A. Carena, M. D. Vaughn, R. Gaudino, M. Shell, and D. J. Blumenthal, "OPERA: An optical packet experimental routing architecture with label swapping capability," *J. Lightwave Technol.*, vol. 16, pp. 2135–2145, Dec. 1998.

[9] H. Yasaka, H. Sanjoh, H. Ishii, Y. Yoshikuni, and K. Oe, "Repeated wavelength conversion of 10 Gb/s signals and converted signal gating using wavelength-tunable semiconductor lasers," *J. Lightwave Technol.*, vol. 14, pp. 1042–1047, June 1996.

[10] S. Hansmann, H. Walter, H. Hillmer, and H. Burkhard, "Static and dynamic properties of InGaAsP–InP distributed feedback lasers—A detailed comparison between experiment and theory," *IEEE J. Quantum Electron.*, vol. 30, pp. 2477–2484, Nov. 1994.

[11] R. Schatz, "Dynamics of spatial hole burning effects in DFB lasers," *IEEE J. Quantum Electron.*, vol. 31, pp. 1981–1993, Nov. 1995.

[12] C. Braagaard, B. Mikkelsen, T. Durhuus, and K. Stubkjaer, "Modeling the dynamics of wavelength tuning in DBR-lasers," *IEEE Photon. Technol. Lett.*, vol. 6, pp. 694–696, June 1994.

[13] B.-S. Kim, J.-K. Kim, Y. Chung, and S.-H. Kim, "Time-domain large-signal analysis of widely tunable DBR laser diodes with periodically sampled and chirped gratings," *IEEE Photon. Technol. Lett.*, vol. 10, pp. 39–41, Jan. 1998.

[14] P.-J. Rigole, S. Nilsson, L. Backbom, T. Klinga, J. Wallin, B. Stalnacke, E. Berglind, and B. Stoltz, "114-nm wavelength tuning range of a vertical grating assisted codirectional coupler laser with a super structure grating distributed Bragg reflector," *IEEE Photon. Technol. Lett.*, vol. 7, pp. 696–699, July 1995.

[15] M. G. Davis and R. F. O'Dowd, "A transfer matrix method based large-signal dynamic model for multielectrode DFB lasers," *IEEE J. Quantum Electron.*, vol. 30, pp. 2458–2466, Nov. 1994.

[16] P.-J. Rigole, "Widely tunable monolithic semiconductor lasers," Royal Inst. Technol., Stokholm, Sweden, Tech. Rep. TRITA-MVT Rep. 1997:2, 1997.

[17] P.-J. Rigole, M. Shell, S. Nilsson, and D. J. Blumenthal, "Fast wavelength switching in a widely tunable GCSR laser using a pulse predistortion technique," presented at the Optical Fiber Communications Conf., Feb. 1997, Paper WL63.

[18] A. Sudbo, "Numerically stable formulation of the transverse resonance method for vector mode-field calculations in dielectric waveguides," *IEEE Photon. Technol. Lett.*, vol. 5, pp. 342–344, Mar. 1993.

Olga Lavrova (S'00) was born in St. Petersburg, Russia, in 1974. She received the B.S. degree in physics and M.S. degree in electrical engineering from the St. Petersburg State Electrical Engineering University.

In 1997, she joined Electrical and Computer Engineering Department of the University of California at Santa Barbara and is currently working towards the Ph.D. degree in the Optical Communications and Photonic Networks Laboratory. Her current work includes experimental and analytical studies of widely tunable semiconductor lasers and their applications in optical network systems.

Daniel J. Blumenthal (S'91–M'93–SM'97) received the B.S.E.E. degree from the University of Rochester, Rochester, NY, in 1981, the M.S.E.E. degree from Columbia University, New York City, in 1988, and the Ph.D. degree from the University of Colorado at Boulder in 1993.

In 1981, he worked at StorageTek of Louisville, CO, in the area of optical data storage. In 1986, he worked at Columbia University in the areas of photonic switching systems and ultra-fast all-optical networks and signal processing. His Ph.D. dissertation topic was in the area of multiwavelength photonic switched interconnects for distributed computing applications. From 1993 to 1997, he was Assistant Professor in the School of Electrical and Computer Engineering at the Georgia Institute of Technology, Atkanta. He is currently the Associate Director for the Center on Multidisciplinary Optical Switching Technology (MOST) and Associate Professor in the Department of Electrical and Computer Engineering at the University of California-Santa Barbara. He heads the Optical Communications and Photonic Networks (OCPN) Research. His current research areas are in optical communications, wavelength division multiplexing, photonic packet switched and all-optical networks, all-optical wavelength conversion, optical subcarrier multiplexing, and multispectral optical information processing. He has authored or coauthored over 80 papers in these and related areas.

Dr. Blumenthal is recipient of a 1999 Presidential Early Career Award for Scientists and Engineers (PECASE) from the White House and the DoD, a 1994 NSF Young Investigator (NYI) Award, and a 1997 Office of Naval Research Young Investigator Program (YIP) Award. He is currently an Associate Editor for IEEE PHOTONICS TECHNOLOGY LETTERS and has served as an Associate Editor for IEEE TRANSACTIONS ON COMMUNICATIONS. He was a Guest Editor for the IEEE JOURNAL OF LIGHTWAVE TECHNOLOGY Special Issue in Photonic Packet Switching Systems, Technologies and Techniques published in December 1998. He is the General Program Chair for the 2001 OSA Topical Meeting on Photonics in Switching and has served as Program Chair for the 1999 Meeting on Photonics in Switching. He has served on numerous other technical program committees including the Conference on Optical Fiber Communications OFC (1997, 1998, 1999, and 2000) and the Conference on Lasers and Electrooptics CLEO (1999 and 2000).He is a member of the Optical Society of America and the Lasers and Electrooptic Society.